Palaeogeography, Palaeoclimatology, Palaeoecology 592 (2022) 110902

Contents lists available at ScienceDirect

Palaeogeography, Palaeoclimatology, Palaeoecology

journal homepage: www.elsevier.com/locate/palaeo

Aeolian imprints of multiple Mediterranean invasions of the Black Sea during Pleistocene

Ahmet Evren Erginal [a,*], Nafiye Güneç Kıyak [b], Özlem Makaroğlu [c], Mustafa Bozcu [d], Muhammed Zeynel Öztürk [e], Haluk Hamit Selim [f], Norbert R. Nowacyzk [g], Nurcan Kaya [c], Tugba Ozturk [h], Mustafa Karabıyıkoğlu [i], Georgios S. Polymeris [j]

[a] Çanakkale Onsekiz Mart University, Department of Geography Education, Çanakkale, Turkey
[b] Istanbul OSLAB- Research & Archeometry Group, Istanbul, Turkey
[c] Istanbul University-Cerrahpaşa, Department of Geophysical Engineering, Avcılar, Istanbul, Turkey
[d] Çanakkale Onsekiz Mart University, Department of Geological Engineering, Çanakkale, Turkey
[e] Omer Halis Demir University, Department of Geography, Niğde, Turkey
[f] Istanbul Gelisim University, Department of Civil Engineering, Istanbul, Turkey
[g] Helmholtz Centre Potsdam, German Research Centre for Geosciences GFZ, Section 4.3 – Climate Dynamics and Landscape evolution, Potsdam, Germany
[h] Isik University, Department of Physics, Istanbul, Turkey
[i] Ardahan University, Department of Geography, Ardahan, Turkey
[j] National Centre for Scientific Research "Demokritos", Institute of Nanoscience and Nanotechnology, Ag. Paraskevi, Athens, Greece

ARTICLE INFO

Editor: A Dickson

Keywords:
Black Sea
Carbonate aeolianite
Ooid
Paleosol
Climate change
Interglacial
Marine isotope stages

ABSTRACT

Climate changes determined the repeated connections between the Black Sea, Caspian Sea and Mediterranean Sea. The landlocked anoxic Black Sea basin was exposed to several transgressions throughout Quaternary by the Mediterranean Sea through the Straits of Istanbul (Bosphorus) and by the Caspian Sea through the Manych-Kerch spillway. Sedimentological records of these connections are limited mostly to the marine terrace deposits of Marine Isotope Stage (MIS) 5e while the pre-MIS 5e period remains uncertain due to a lack of robust facies and chronological data from deep-sea sedimentary sequences. Here we discuss the imprints of multiple Mediterranean transgressions during Middle Pleistocene in the Black Sea based on facies analysis and the optical age of coastal carbonate aeolianites. Contrary to today's hydro-climate of the Black Sea, the aeolianites bear witness to the transformation of the Black Sea into a warm inland sea during successive Mediterranean invasions. Prior to the onset of aeolian deposition, paleosols were formed on the Eocene-aged hardened sandy silts, suggesting strongly washed soil. This is evidenced by no calcium carbonate and a high Rb/Sr ratio, with quartz amounting to of 99.8%. According to our OSL ages, carbonates deposited on the shelf plain under higher temperature and increased evaporation conditions in MIS 15 and the later interglacial phases were transported to the coastal sand dunes during the transitional phases of MIS 15–14, MIS 13–12, MIS 11–10 and MIS 9–8. We suggest that the carbonate-rich and ooid-containing aeolianites were repeatedly formed in the multiple Mediterranean transgression stages, beginning with an increasingly severe dry phase following the Brunhes-Matuyama magnetic reversal.

1. Introduction

The successive bilateral invasions of the Black Sea (BS) by the Mediterranean (MS) and Caspian (CS) seas have been decisive regulators of the Black Sea's water level throughout its Quaternary history. Reconnections during the interglacial periods and ensuing disconnections in glacial times caused recurrent changes in the salinity, temperature and paleoecological conditions of the BS, leading to the emergence of different Pleistocene basins since Gurian (Fedorov, 1978; Yanko-Homback et al., 2017) over the last 1.1 ma. In relation to these Pleistocene basins, the best recognized period in the Quaternary geochronology of the Black Sea is the last MIS 5 interglacial, dominated

* Corresponding author.
E-mail addresses: aerginal@comu.edu.tr (A.E. Erginal), ozlemm@istanbul.edu.tr (Ö. Makaroğlu), nowa@gfz-potsdam.de (N.R. Nowacyzk), tozturk@isikun.edu.tr (T. Ozturk), g.polymeris@inn.demokritos.gr (G.S. Polymeris).

https://doi.org/10.1016/j.palaeo.2022.110902
Received 26 December 2020; Received in revised form 7 December 2021; Accepted 27 February 2022
Available online 4 March 2022

by increased salinity of the BS linked to the inflow of MS waters (Svitoch et al., 2000), albeit from limited reliable chronological data. The MIS 5e interglacial is characteristically confirmed by the age of marine shells near the Taman Peninsula and the Kerch Strait to the north (Arslanov, 1993), aeolianites as terrestrial equivalents to the west of Şile on the West Black Sea coast of Turkey (Erginal et al., 2013), and multi-proxy data from a 9.45 m-long sediment core on the southern shelf of the BS (Wegwerth et al., 2014).

Regarding the pre-MIS 5e history of the BS, data on paleoenvironmental geographical conditions during the transitions from interglacial to glacial is quite controversial and limited. The lack of relevant chronological data from deep-sea sequences increases the importance of correlative terrestrial coastal deposits for understanding the multiple MS invasions of the BS. Marine terrace deposits on the central and eastern BS coasts of Turkey yielded ESR ages of 407.998 ± 67.475 ka (Keskin and Pedoja, 2011) and OSL ages of 638 ± 59 ka (Yildirim et al., 2013), respectively. The only perpetual chronology is, on the other hand, based on oxygen isotope ($\delta^{18}O$) signatures from Sofular Cave in NW Turkey, proving that BS-MS connections have been established at least 12 times in the last 670,000 years (Badertscher et al., 2011).

In cores obtained from offshore shelf levels in the northwest part of the Bosphorus, terrestrial muds form the most up-to-date unit on the seafloor, accumulated in the interglacial and glacial periods of the last 700,000 years, marking the Brunhes-Matuyama transition (Hsü and Giovanoli, 1979). The only carbonated unit is comprised of Messinian sediments, which are represented by stromatolitic dolomite, oolithic sands and calcarenites, as well as coarse gravels located at a depth of 864–884 m (Hsü and Giovanoli, 1979; Gillet et al., 2007). In other words, the sedimentary records of the interglacial and glacial phases in the Black Sea bottom over the last 700,000 years have not provided satisfactory sedimentological information to distinguish interglacial and glacial times.

An impressive succession of carbonate cemented, transgressive aeolian sandstones consisting of mixed siliciclastic (quartz-rich) sands and oolithic carbonates are well-exposed on a series of steep-faced cliffs 9 m high in places along the NW-SW oriented western coastal zone of Şile (Fig. 1a,b). These aeolian sandstones, aeolianite sensu stricto, unconformably overlie more than 1.5 m thick, massive, quartz-rich terra rossa type paleosols with a sharply defined, slightly erosional flat contact and also the basement rocks further inland. In turn, the aeolian sandstones are overlain by a relatively-thin cover of modern climbing aeolian sands in places.

The relationship between the deposition of aeolianite sands and binder carbonates and sea level changes during glacial and interglacial stages has actually been known since Darwin's first observations on St Helena Island (Darwin, 1841), and is still a matter of debate. According to Darwin, these formations are a remnant of the sand dune systems that existed on the coast while a shallow shelf existed around the island

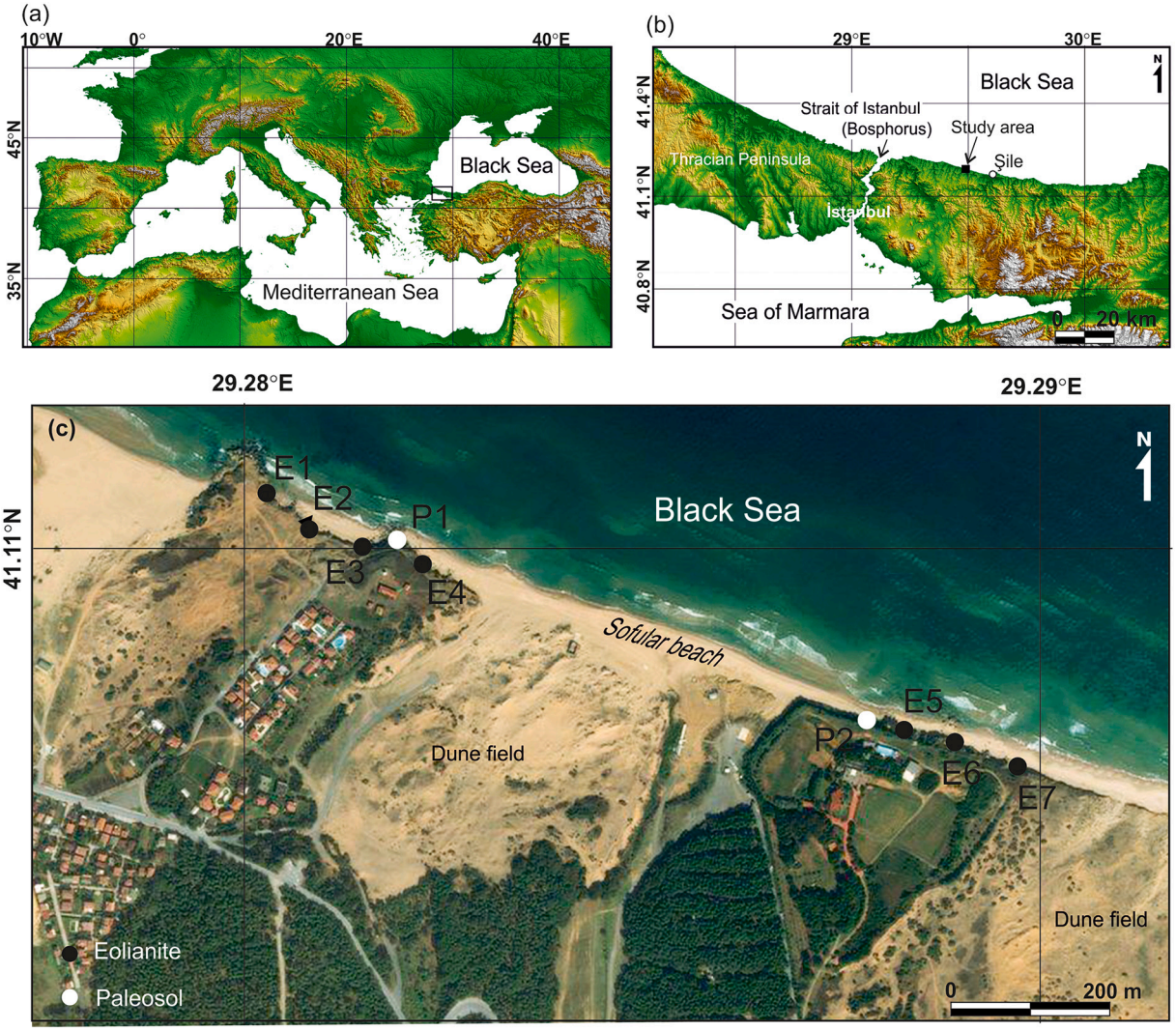

Fig. 1. Location map of study area (a,b) and sampling sites (c) on GoogleEarth image.

under low sea level conditions. Daly (1925), who made later observations on this island, determined that these sediments were also found at a depth of 20–30 m off the coast, and based on this, he stated that even a very small decrease in sea level would lead to the transport of sediments to the coast. Sayles (1931), who gave an important explanation for the formation of aeolianite, drew attention to the relationship between aeolianite formation in Bermuda and the ice ages; that aeolianites were formed by the transport of shelf sediments to the dunes, that paleosols were associated with sea level fluctuations during the ice ages, and that these clay-rich fossil soils indicated moist interglacial periods.

Aeolianites in the Bahamas belong to the interglacial periods with a high sea level (Carew and Mylroie, 1997; Hearty and Kindler, 1997). Likewise, the aeolianites of the Coorong Region in the southeastern part of Australia (Murray-Wallace et al., 1998, 2001)and the aeolianites of the Western Mediterranean coast (Fumanal, 1995) are typical examples of this group (Brooke, 2001). In contrast, chronostratigraphic evidence from large dune systems has been found on the southwest coast of Australia (Kendrick et al., 1991; Price et al., 2001), the Hawaiian and California Islands (Muhs et al., 1993) and off the coast of Israel (Porat and Wintle, 1995; Engelmann et al., 2001; Frechen et al., 2001) reveal that the aeolianites belong to the ice age.

This study discusses for the first time the successive reconnections of the BS with the MS based on description and interpretation of a process-oriented study of facies and depositional architecture. The chronology of the carbonate-cemented coastal aeolianites is an important aspect of the present study; ages were calculated using optically stimulated

Fig. 2. Sampling sites of aeolianite. Black dots and numbers indicate locations of samples collected for petrographic analysis and OSL dating. White dots and numbers indicate locations of samples collected for paleomagnetic analysis. Hammer for scale is 33 cm long.

luminescence (OSL) and paleomagnetic measurements. Many studies have shown that sand grains are very effectively zeroed during wind-blown transportation and it can be confidently expected that this applies to the material examined here (Sivan and Porat, 2004; Roberts et al., 2008; Fornos et al., 2009). Several laterally-continuous sections characterized by distinct stratification in the exposures, with orientations running both parallel and perpendicular to the aeolian transport direction, have provided an excellent setting for studying facies and depositional architecture. The studied aeolianites, as well as the cemented coquinites in the nearby region, are the only Middle to Late Quaternary units in the coastal zone and no tectonically-induced deformation was observed in this region (Erginal et al., 2017), which is tectonically calm compared to the seismicity of Southeast Crimea, Georgia mainland, offshore in Bulgaria, and at Bartın on the Black Sea coast of Turkey (Kalafat, 2017).

2. Methods

2.1. Field studies, sampling and analyses

Stratigraphic and sedimentological observations were made at Şile, located between 41°11′29″ N and 41°1114″ N latitudes and 29°2847″ E and 29°2935″ E longitudes, along an 800 m-long outcrop in order to determine the bedding geometries, changes in sequence thickness, contact relationship with the underlying paleosol unit, lateral extent of the aeolianite, and bounding surfaces from bottom to top. Bedding measurements were carried out at 230 different sections to understand the direction of transport of aeolian sands by paleowinds. The measurements were carried out separately in the western and eastern parts of the aeolianite sequence because the aeolianite, which forms an outcrop totalling 800 m, is currently divided into two parts by a 1 km-wide coastal dune area. A total of 21 rock samples and two paleosol samples were collected for analysis and dating from 9 typical sections where the aeolianite offers continuous outcrops (Figs. 1c, 2).

Mineralogical and petrographic descriptions were made by petrographic thin sections of the rock samples. With SEM (Scanning Electron Microscopy) and EDX (Energy Dispersive X-Ray Spectroscopy) analysis, the crystal morphology, sequential cement structures, element compositions, texture properties and the shape and size of the cemented grains were examined. Mineral composition of the aeolianite and paleosol samples was determined by X-ray diffractometry analysis. The total $CaCO_3$ was measured with a Scheibler calcimeter. Element analyses were performed using ICP-MS in ACME Laboratories (Canada) to determine the geochemical composition of the aeolianites and paleosols.

2.2. OSL age assessment (handling, chemical treatment, luminescence apparatus and protocol)

2.2.1. Rationale

The OSL technique was first proposed by Huntley (1985) and was later developed further (Banerjee et al., 1999; Murray and Wintle, 2000; Liritzis et al., 2013a; Li and Li, 2019). For calculating OSL ages, two quantities are required, namely, the equivalent dose (De) as well as the environmental dose rate (DR). De corresponds to the radiation dose absorbed since the last exposure of the material to light and is measured using the OSL technique. The other parameter required to calculate the OSL age, namely, the dose rate (DR), is calculated using the concentrations of U, Th and K reflecting the radioactive content within the sample and in the environment, plus the dose rate derived from cosmic radiation. Thus, the OSL age (in ka) was found through the ratio between the equivalent absorbed dose (in Gy) and the radiation dose rate (in Gy/ka) according to the following equation:

$$\text{OSL age} = \text{Equivalent Dose (De)}/\text{Radiation Dose Rate (D)} \quad (1)$$

where the equivalent dose is measured in (Gy) and the radiation dose rate in (Gy/ka), resulting in the OSL age in (ka).

2.2.2. Handling and chemical treatment

For OSL analysis, the outer parts of light-subjected surfaces were cut and removed and the remaining inner portion was crushed and powdered. Handling was performed under dim red-light conditions (620–640 nm). Before the OSL measurements and after crushing, the following sequential steps were performed:

Step 1: Chemical reaction with hydrochloric acid (10%) to remove carbonates.

Step 2: Chemical reaction with hydrogen peroxide (35%) to remove organic material (fresh hydrogen peroxide was continuously added until the chemical reaction occurred).

Step 3: Wet sieving towards obtain grains with a dimension of 90–140 μm.

Step 4: Treatment with hydrofluoric acid (40%) for 45–60 min.

Step 5: Final treatment with hydrochloric acid (10%) to obtain a clean quartz extract.

Step 6: Washing using distilled water and subsequent drying in an oven at 50 °C.

Step 7: Preparation of aliquots with mass of around 5–7 mg each (corresponding to 700–1200 grains for this specific grain size fraction), by mounting the material on stainless-steel disks using silicon spray.

2.2.3. Luminescence apparatus

All OSL measurements were conducted at the Luminescence Research and Archeometry Laboratory at Istanbul, Turkey, using a Risø TL/OSL reader (model TL/OSL-DA-15). This reader is equipped with (a) a $^{90}Sr/^{90}Y$ beta source, providing a dose rate of 89 ± 4 mGy/s, (b) a 9635QA photomultiplier tube that was used for light detection, (c) detection optics consisting of a 7.5 mm Hoya U-340 filter (λp ~ 340 nm, FWHM ~80 nm), with a peak transmission at around 340 nm, (d) blue LEDs for stimulating quartz, with stimulation wavelength 470 ± 20 nm in the case of blue stimulation, delivering at the sample position a maximum power of ~24 mW/cm^2 and (e) an infrared solid state laser (880 nm, FWHM 75 nm, maximum power 135 mW/cm^2) (Bøtter-Jensen, 1997; Bøtter-Jensen et al., 2000). Preheating was performed in a nitrogen atmosphere with a low constant heating rate of 2 °C/s to avoid significant temperature lag (Kitis et al., 2015). Examination using infrared stimulation at the ambient temperature indicated the presence of clean quartz populations, as it was revealed by either the lack of an IRSL signal or ratio values of IRSL over OSL, being lower than 1% (Murray et al., 2015).

2.2.4. Equivalent dose

In the present study, the chemical treatment focused on the isolation of quartz. Therefore, stimulation includes solely blue light at the continuous wave configuration (CW – OSL) for 50 s at 125 °C, as it is adequate to totally deplete all optically sensitive traps for each regeneration dose. The experimental protocol that was applied for the calculation of the equivalent dose (ED hereafter) is presented in tabulated form below (Table 1).

This is a typical version of the single aliquot regenerative-dose (SAR) protocol, firstly introduced by Murray and Wintle (2000, 2003), and following modifications suggested by Banerjee et al. (1999, 2001). It includes eight cycles; one for the natural OSL signal, five cycles with increasing regenerative doses, one zero-dose recuperation cycle, and a final recycling ratio cycle, involving the lowest regenerative dose. The regenerative doses were 15, 35, 70, 130 and 200 Gy. Regenerative doses were chosen within the range in which the natural dose point falls. After each regenerative dose, the sample was preheated at 260 °C for 10 s to remove unstable OSL components; this preheating temperature was selected according to preliminary preheat plateau tests. Sensitivity changes were both monitored and corrected with the aid of a test dose of 15 Gy, delivered after each regenerative, natural, and zerodose OSL measurement following a cut-heat temperature of 180 °C for the same

Table 1
Steps of double SAR protocol applied in present study.

Step no	Action	Comments & Technical Specifications
1	Give regenerative dose, D_i	*$D_1 = 0$ Gy (Natural), D_2-D_6 Regenerative doses (15, 35, 70, 140, 200 Gy), $D_7 = 0$ Gy (Recuperation), D_8=D_3 (Recycle point)*
2	Preheat	*Duration 10 s, Temperature 260 °C*
3	CW-OSL measurement	*Duration 50 s, Temperature 125 °C: Natural & regenerative OSL measurement L_i*
4	Give test dose, D_i	*$D_t = 15$ Gy*
5	Cut-heat	*Duration 10 s, Temperature 180 °C*
6	CW-OSL stimulation	*Duration 50 s, Temperature 125 °C: Test dose OSL measurement L_t*
7	Return in 1 for a fresh sample	*Each measurement cycle was repeated for (at least) 15 different aliquots.*

reason as the preheat treatment. Using the corrected dose points, a growth curve was constructed to estimate the equivalent dose by interpolating the natural OSL dose point over the curve for each one of aliquots measured. At least ten aliquots were measured for each sample. The zero regenerative dose taken was used to observe the bleachability of the samples as well as whether the dose response curves go through the origin of the axis.

2.2.5. Dose rate

The dose rate was calculated according to the content of natural Uranium (including both ^{235}U and ^{238}U), ^{232}Th and ^{40}K radioactive isotopes plus the contribution of the cosmic rays. Portions of each bulk sample were submitted for Induced Coupled Plasma mass spectroscopy (ICP-MS, Acme Analytical Laboratories Ltd., Vancouver, Canada). Dose rates were calculated from these concentrations using the dose rate conversion factors of Liritzis et al. (2013b). External alpha contribution to the dose rates was ignored because the quartz grains were etched by HF treatment, as described above. The contribution of cosmic radiation to the dose rate was calculated using the sampling depth, elevation and geographical positions (Olley et al., 1996; Prescott and Hutton, 1988, 1994).

In addition, another portion of the sample material was used to determine the moisture and carbonate content affecting dose rates. As any sample is considered to be composed of three components, namely mineral (m), organic (o) and water (w), dose rates were corrected for organic and water following the methodology of Lian et al. (1995). Finally, the model of Nathan and Mauz (2008) was applied in order to correct the dose rate for the impact of carbonated cement. Due to dissolution and re-precipitation, the dose rate is not stable in the long-term; thus, modelling these is important in carbonate-rich deposits.

2.3. Paleomagnetic measurements

Paleomagnetic dating is a very useful technique to date Quaternary sediments and is widely used on different sedimentary units (Dirks et al., 2010; Pappu et al., 2011). For our paleomagnetic analysis, a total of 57 oriented cylindrical samples were collected from 14 different layers varying between 10 and 90 cm intervals through a 500 cm profile to date the aeolianite unit (Fig. 3). The cylindrical samples were cut into 97 standard paleomagnetic sub-samples. We also took continuous samples 100 cm long through the paleosol unit at the bottom of the aeolianite unit. All measurements were performed at the paleomagnetic laboratories of GFZ in Potsdam and at Istanbul University. A JR-6A spinner and 2G Enterprises 755R three-axis DC-SQUID cryogenic magnetometer were used to measure the natural remanent magnetization. Alternating field (AF) demagnetization with an amplitude up to 100 mT was performed by a LDA-3A and a 2G-Enterprises degausser attached to the magnetometer.

Principal component analysis (Kirschvink, 1980) and Fisher statistical analysis (Fisher, 1953) were used to define the vector components and the average ChRM, respectively. Rock magnetic analysis, including acquisition of isothermal remanent magnetization (IRM) and three component-IRM thermal demagnetization experiments (Lowrie, 1990), were conducted on a selected sample from every layer. To identify the magnetic carriers, based on their coercivities and unblocking behaviour, the stepwise acquisition of IRM was applied up to 1 T along the sample z axis (hard component), 0.4 T along the sample y axis (for medium component), and 0.12 T along the sample x axis (soft component)

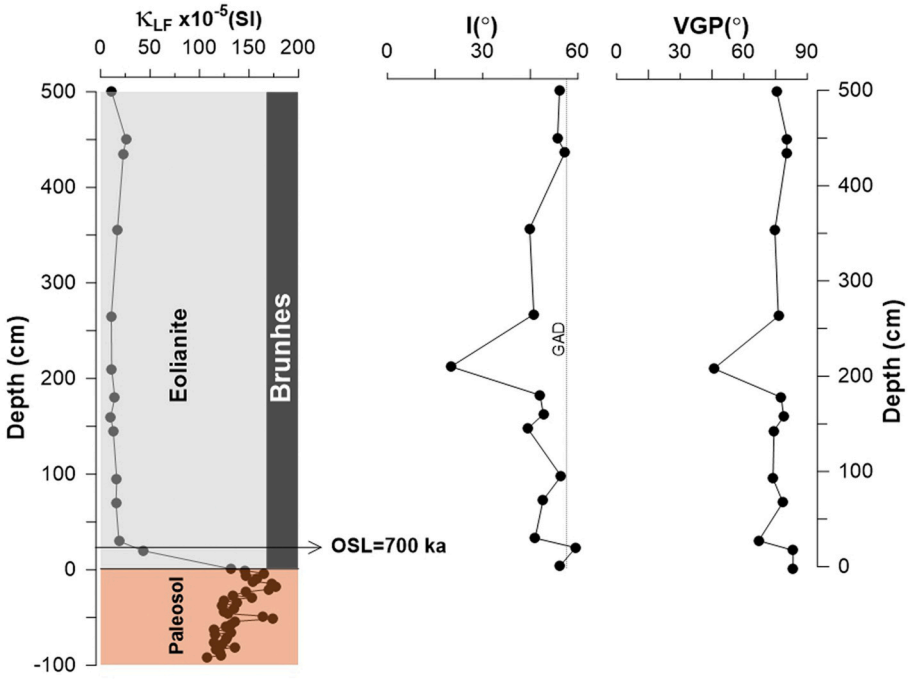

Fig. 3. Magnetic susceptibility profile of aeolianite and paleosol units in studied area and paleomagnetic directions (I, VGP) of aeolianite unit. κ_{LF} (low field magnetic susceptibility), GAD (Geocentric Axial Dipole), VGP (Virtual Geomagnetic Dipol), and I (Inclination).

(Lowrie, 1990). The IRM was performed with an ASC pulse magnetizer. Magnetic susceptibility measurements were performed by an AGICO-Kappabridge susceptibility meter (MFK-1S). The thermomagnetic experiment measured a representative sample from the aeolianite unit by heating it in air at room temperature up to 600 °C using AGICO LY-2 Kappabridge.

3. Results

3.1. Composition of aeolianite

The total calcium carbonate content in the Şile aeolianite ranges between 61.5% and 94.6%, therefore revealing that it can be defined as carbonate aeolianite (Fairbridge and Johnson, 1978; Abegg et al., 2001). Well-sorted laminated sands, with no grains of a size up to 3 mm, are also suggestive of aeolian carbonate sand dunes in petrographic composition. Two important components of the carbonate composition are ooids and binding minerals, consisting of calcite and aragonite (Fig. 4). XRD analysis showed that the amount of quartz ranged from 5.4% to 38.5%.

Thin section and electron microscopy analysis revealed the existence of almost the same mineralogical and petrographic properties in all samples. The framework grains are polycrystalline quartz, epidote, ooid, plagioclase and partially-opacified calcite and aragonites. Ferromagnesian minerals (biotite, pyroxene, augite, etc.) as accessory minerals and rock fragments (chert), derived from various origins, comprise the other constituents. Spar calcite cement and meniscus bridges are common. Opacifications on the walls of ooids and other grains may be due to the effect of atmospheric conditions. Indeed, there are traces of etching on the calcite surfaces. The nuclei of some ooids have disappeared due to erosion, especially in elliptical and flat-shaped ooids. Generally, the external cortex comprises fibrous aragonite crystals that form envelopes. In some examples with no nuclei, the aragonitic needles in the laminae forming the ooid cortices have been preserved. Some of the ooids are made up of polycrystalline quartz. It is seen that some ooids have a thick cortex, where the thickness of the cortex is much higher than the core thickness and the spaces between the ooids are filled with calcites that increase in size towards the centre.

3.2. Facies architecture

A description and interpretation of the process-oriented study of facies and depositional architecture in the coastal aeolian succession is presented and evaluated here. Several laterally continuous sections, characterized by distinct stratification types with orientations running both parallel and perpendicular to the aeolian transport direction, provide an excellent setting for studying the facies and depositional architecture. This enables valuable insights with which to make reliably sound inferences on understanding the three-dimensional reconstruction of genetically-related aeolian dune and interdune deposits and the associated spatial and temporal changes in the evolving pattern of this coastal dune system.

In the exposed sections, three distinct lithofacies are recognized, based mainly on primary sedimentary structures and the geometry of distinct stratification types, in particular pin-stripe (wind ripple, translatent) laminae, which are considered to be critically important characteristics for identifying and understanding ancient aeolian dunes, their morphology and style of deposition (Hunter, 1977; Fryberger, 1979; Fryberger and Schenk, 1988; Bristow and Mountney, 2013). These facies are defined here in simple terms on the basis of their prominent stratification type as 1) horizontally-stratified aeolianite facies, 2) cross-stratified aeolianite facies, and 3) deformed aeolianite facies, respectively (Fig. 5).

3.2.1. Horizontally-stratified aeolianite facies

This unit forms the lowest visible level of the section and its thickness ranges from 1 to 1.6 m. This facies is represented by horizontal to sub-horizontal tabular-planar sets of aeolianite which are bounded sharply by horizontal to gently inclined, planar or slightly undulating surfaces. These sets are about 20 to 50 cm thick and consist of thin to thick, plane-parallel laminae with a thickness of several mm and beds of 1–3 cm. The layers in the planar-tabular cross-layered sets are generally inclined to the east and southeast. Dip angles vary between 10° and 15° in the upper parts, which decrease gradually towards the base of the unit and gain a near-horizontal angle with a concave appearance at the bottom. This laminated basal unit has very low angle southwest inclinations (2°-5°) and consists of very fine sandstone-silty to very fine sand alternation. The unit is predominantly composed of a mixture of moderately- to well-sorted, very fine to coarse-grained (1–0.065 mm), angular to sub-rounded quartzite sands and ellipsoidal to well-rounded oolithic

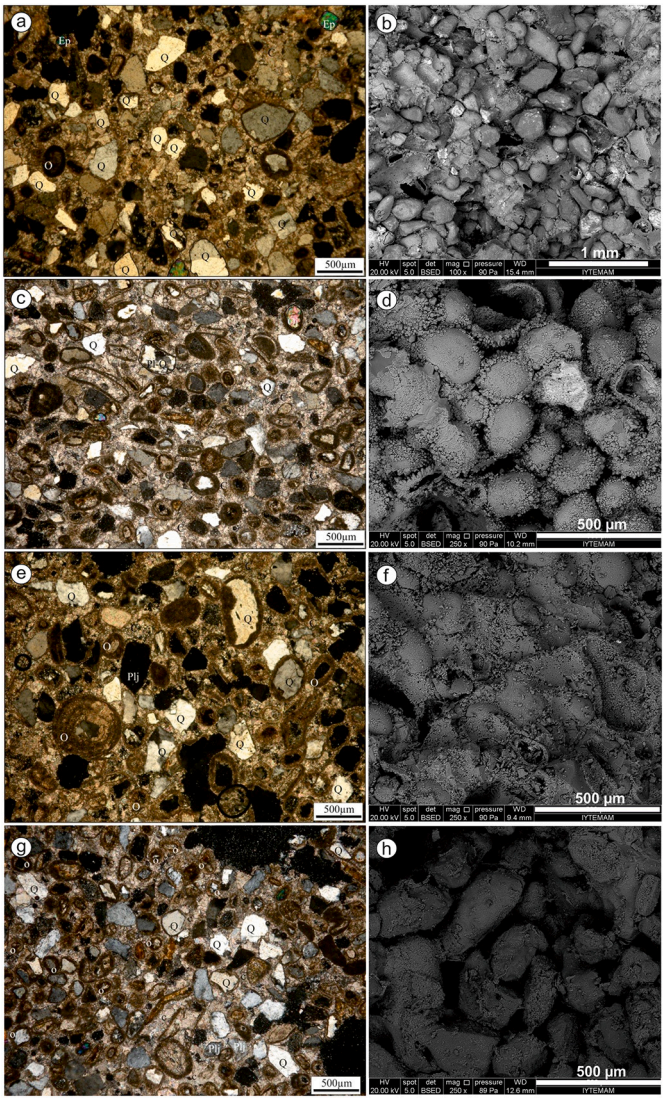

Fig. 4. Thin section micrographs and SEM images of representative samples of aeolianite. (a,b) quartz arenite, including angular chert fragments, quartz (Q), plagioclase (plj), epidote (Ep), augite and opaque minerals; (c,d) ooid sandstone, including spear-shaped aragonite crystals growing on grain surfaces or towards the nucleus of empty ooids, opacification, polycrystalline quartz; (e,f) sandstone with ooid, angular and slightly round monocrystalline and polycrystalline quartz, opacified ooids on walls, opacified calcite and aragonite crystals on walls of the grains, and meniscus-type spar calcite cement; (g,h) ooid sandstone, ooids with nuclei usually composed of quartz fragments, angular semi-angular quartz grains, calcite and ferromagnesian minerals (augite), spar calcite cement, opaque in the envelopes of ooids and edges of some grains.

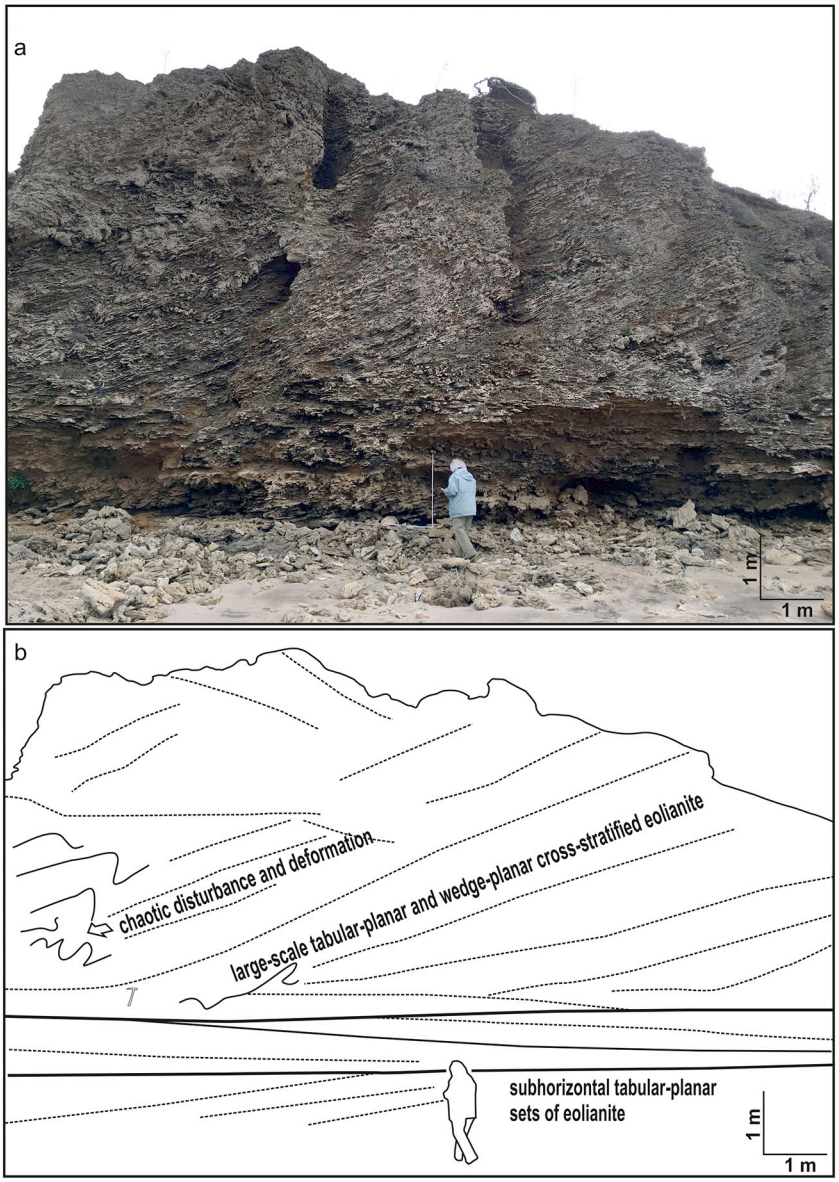

Fig. 5. (a, b) Characteristic sedimentary properties of aeolianite. Man for scale is 1.56 m.

carbonates.

This unit, whose upper surface is defined by a first-degree flat surface boundary, generally reflects the lower part of a coastal sand dune extending in a SE direction and whose upper part is abraded. In this context, the 1st degree surface boundary lying flat on the sand dune indicates a sand surface created by erosion. Evenly plane-parallel laminated and moderately-sorted horizontal tabular sets of this facies represent interdune sediments that probably developed on the flat to gently sloping surface of an area of flat sand sheets (Hunter, 1977; Kocurek and Dott, 1981; Lancaster and Teller, 1988). Relatively thinner, finer and well-sorted sub-horizontal laminae may represent deposition resulting from climbing translatent strata formed by migrating wind ripples.

3.2.2. *Cross-stratified aeolianite facies*

This facies is characterized by medium and large-scale tabular-planar and wedge-planar cross-stratified yellow sandstone with fine to medium grained and well-sorted quartz and oolithic grains. Cross-strata are arranged in 1–5 m thick, solitary or superimposed tabular sets which are delimited abruptly at the base and on the top by sharply defined horizontal and gently-inclined planar surfaces which can be traced laterally at the exposures. Cross-stratification is represented by high angle inclined (15° to 30°) oblique-parallel and slightly concave upward foresets which consist of thin to thick fine-grained laminae and very thin beds. The laminae and the beds downlap to the base marked with sharply defined angular contact or tangentially (asymptotically) with gently inclined or slightly curved (concave up) laminae and toplap with angular contact to the upper bounding surface. The dip directions of the foreset laminae are mainly northwest, south and southeast.

Tabular-planar and wedge–planar cross-stratified sets, with steeply dipping foreset laminae and sharply defined angular and tangential lower contacts and flat to inclined truncated tops, represent the preserved parts of large scale two-dimensional and three-dimensional advancing transverse dunes with erosion on the stoss-side and net deposition on the lee-side (Rodríguez-López et al., 2014). Steep to low angle inclined foreset laminae represent the construction and preservation of the dune system through continuous sedimentation on the dry and non-cohesive slip faces exceeding the critical angle of repose of the grains by avalanching processes, grain flows of non-cohesive sands, and grain falls, respectively (Hunter, 1977; Kocurek and Dott, 1981).

Sharply-defined horizontal and gently-inclined lower and upper boundaries are the first order bounding planar surfaces. The truncation of the foreset laminae (steeply inclined slip faces) at the top indicates a period of sediment starvation and wind erosion related to changes in the prevalent wind direction and the cessation of dune migration. The dip directions measured from the tabular cross-stratified foresets indicate that the orientation of the dunes was determined by south-easterly, northerly and north-westerly paleowinds. The surface boundaries occur due to changes in wind direction and velocity during dune progression, documenting pauses during sand dune migration, direction changes in the dune, and erosion on the dune surface.

3.2.3. *Deformed aeolianite facies*

This facies is represented by slightly to chaotically disturbed post-depositional structures and impressions of footprints and burrows on various scales that are exhibited both in the cross-stratified and evenly parallel-laminated horizontal deposits. Chaotic disturbance and deformation specifically occur in large-scale cross-stratified yellow calcareous aeolianites which are characterized by pin-stripe like, fine grained and steeply inclined foreset laminae. Deformed structures include intricately folded, buckled, wrinkled laminae, intraformational rip-up clasts and massive, sub-rounded to rounded lumps of silty fine sand. Impressions of footprints, characterized by downward inverted deformations and animal burrows occur commonly on the bedding planes of the subjacent parallel laminae in the horizontal and sub-horizontal sets.

The chaotically disturbed and intricately contorted laminations with massive sandy lumps and intraformational rip up clasts of this facies represent penecontemporaneous hydroplastic deformation on the steep lee side of the migrating dunes, resulting from aerially-limited sand flows due to slope failure under wet conditions after heavy rains or snow melts as the increased amount of intergranular pore water negatively effects cohesiveness of the sandy sediments (Bigarella, 1972; McKee and Bigarella, 1972). Footprint impressions, which occur specifically within the horizontal and sub-horizontal sets, are also indicative of moist sand.

3.3. *Paleosols*

Paleosols, which hold concrete records of the climatic conditions and pedogenic processes of the period in which they were formed, are indicators of the tendency towards humid and rainy climatic conditions following the wind-blown drift and accumulation of aeolian sands in drier periods. In many studies of aeolianites along coastlines around the world, paleosols have been found in colours and compositions quite similar to those in the research area. Some examples of these are the Southwest Cape in South Africa (Butzer, 2004), Karmel Coast in Israel (Tsatskin and Ronen, 1999; Sivan and Porat, 2004), the Gulf of Haifa (Tsatskin et al., 2015), on the Gaza Strip Coastal plain in Palestine (Zaineldeen, 2010), Rottnest Island on the west coast of Australia (Hearty and O'Leary, 2008), on the Xisha Islands in the South China Sea (Zhao et al., 2011), Bermuda Island (Hearty and Vacher, 1994; Herwitz et al., 1996; Muhs et al., 2012; Rowe and Bristow, 2015), the northwestern coast of Egypt (El-Asmar and Wood, 2000), on the eastern coast of Tunisia (Frébourg et al., 2010), the Channel Islands in California, USA (Muhs et al., 2009), Hawaii (Fletcher et al., 2005), the Bahamas Islands (Foos, 1991; Kindler and Hearty, 1995; Carew and Mylroie, 2001), Lord Howe Island (Brooke et al., 2003), and the east coast of Australia. These are among the main locations where paleosols have been detected.

In the present study, two brown reddish paleosol horizons, varying in thickness from 20 cm to 50 cm, were typically observed and collected in two different sections. Sampling locations and the location of the paleosols (P1 and P2) are shown in Fig. 6. These samples were taken at 1 m and 5 m depth from the surface, respectively. Sample P1 is a red colour; it exhibits a wavy surface on the solid-looking sand facies at the bottom and ends with laminated aeolianite layers on the top. The pH is 9.7 and the calcium carbonate is almost completely washed away from the medium (0.28%), confirmed by the small amount of Sr (18.7 ppm) and Ca (0.47%) in contrast to the excess of Rb, Zr, Fe and K (Table 2). In chemical decomposition, it is known that the elements Ca and Sr move away from the environment faster and more effectively than K and Rb; this leads to enrichment in terms of K and Rb and depletion in terms of Ca and Sr (Xu et al., 2010). The Rb / Sr ratio, which is one of the most commonly-used indices to measure paleopedogenic soil processes and weathering intensity, was evaluated here based on the paleosol samples. A high Rb / Sr ratio in loess paleosol sequences has been linked to a more effective weathering rate (Chen et al., 1999) because Sr is removed from the soil due to an increase in weathering. The Rb / Sr ratio in P1 is quite high (0.47), signifying that it represents a fossil soil formed under more humid and rainy conditions. According to our XRD analysis, 98.4% of the mineral composition of the paleosol is quartz, 0.7% is cadmium cyanide, and 0.9% is zeolite.

Sample P2, lying at a depth of 5 m below the surface, is quite different from P1. With a thickness of 25 cm, the paleosol is dirty yellow in colour and closer to the aeolianite on which it developed. Contrary to P1, it contains more $CaCO_3$ (16.43%), Sr (69.2 ppm) and Ca (4.45%). Rb, Zr, Fe, Al and K ratios are close to the P1-coded sample. The higher amount of $CaCO_3$ and Sr, as well as the lower Rb/Sr ratio (0.03), reveals that this paleosol was formed under lower humidity and precipitation

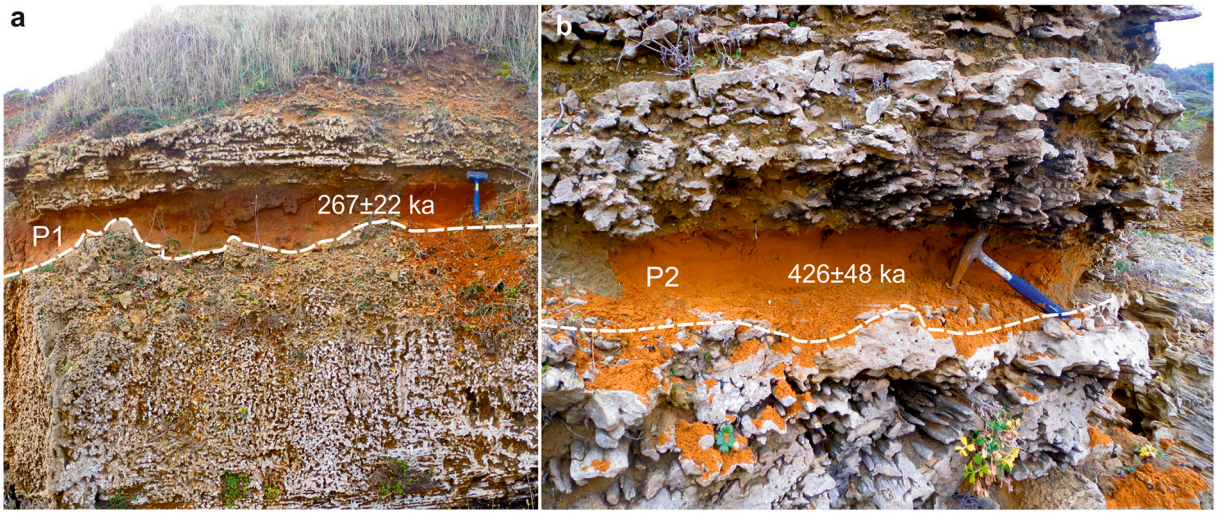

Fig. 6. (a, b) Views of paleosol units within aeolianite beds. Hammers for scale are 28 cm (a) and 33 cm (b) long.

Table 2
Paleosol analysis results.

Sample code	Depth (cm)	$CaCO_3$	C_{org}	pH	Rb (ppm)	Sr (ppm)	Zr (ppm)	Fe (%)	Ca (%)	K (%)	Rb/Sr
SP1	100	0,28	0,43	9,7	8,8	18,7	4,0	1,73	0,47	0,11	0,47
SP2	500	16,43	0,43	9,9	2,1	69,2	2,8	1,00	4,45	0,03	0,03

conditions. XRD analysis demonstrated the presence of quartz (67.6%), calcite (20.6%), potassium cyanide (3.2%) and zeolite (8.6%).

3.4. Paleomagnetic records

The magnetic susceptibility profile distinguishes the physical properties of the aeolianite and paleosol units very clearly, as does the lithological description (Fig. 3). The IRM curve shows low coercivities, saturated below the 0.3 T field. The three component-IRM thermal demagnetization experiments show that the studied aeolianite unit consists of a dominant low-coercivity (0.12 T) magnetic phase with a maximum unblocking temperature of 450 °C, signifying the presence of fine-grained magnetite. Temperature-dependent magnetic susceptibility measurement of the selected aeolianite sample shows a Curie point at 580 °C, indicating the presence of ferrimagnetic minerals, of which magnetite is dominant.

The NRM intensities of the samples, except for samples from layer L1 taken from the boundary of the paleosol and aeolianite with an average value of 28.65 mAm^{-1}, range from 0.88 to 11.5 mAm^{-1}, with an average of 3.2 mAm^{-1}. The degree of inclination, ranging from 59.3° to 20°, shows positive polarities. The average MAD values of 5.15° indicate well-defined ChRM directions for the studied aeolianite samples. The demagnetization steps of the samples show a clear normal polarity, with northward declination and downward inclination. The obtained $D/I = 16.6°/54.2°$ from the top of the studied section is consistent with the present Geocentric Axial Dipol (GAD), which is $D/I = 5.21°/58.03°$ for the studied site. The studied aeolianite unit preserves only normal polarity and no layers in reverse. All VGPs were located at the North Pole, which indicates a normal polarity chron.

3.5. Luminescence features and age calculations

Table 3 presents all the data required for the calculation of the OSL ages of all sediments. Organic content was calculated to be less than 3% while the present water content was calculated as between 5 and 11%. The equivalent doses are quite large, yielding a minimum value of 100 Gy and even larger, with high precision. For all SAR dose response curves, saturating exponential expressions were used. It is important to note that the regenerative doses are quite large, despite the generally low saturation level of quartz. According to a previous study on other Şile aeolianites (Polymeris et al., 2012), local quartz samples indicate quite high levels of saturation, while the linearity reaches up to almost 100 Gy. As this latter figure indicates, the dose response curve passes through the origin, due to a recuperation level of roughly 7–12%; this was the case for the majority (>92%) of the aliquots. In general, aliquots were accepted for analysis if they met criteria for the detectable net natural test signal (greater than three sigma above the background signal), recycling ratio values less than 10%, recuperation values less than 15% and an effective sensitization correction procedure (average value within 1 ± 0.2 in all test doses for each sample). Low regeneration values could also be attributed to the presence of a well defined fast OSL component in the OSL decay curves of the quartz that is the subject of the present study.

It is important to note that the geochemistry of the samples was calculated using a small quantity from the bulk polymineral material (i.e., including both $CaCO_3$ and quartz from the sediment) using ICP-MS. Dose rates were calculated from these concentrations using the dose rate conversion factors of Liritzis et al. (2013a, 2013b). The content of these radionuclides is very low, resulting in very low dose rates. The term "conventional age" in Table 3 was adopted for the age that was obtained under the assumption that the dose rate is constant. Nevertheless, as the content of calcium carbonate within the samples exceeds, the conventional dose rate calculations consider air and water as a constant pore-filling substance and account for the attenuation effect of water, using correction factors proposed by Zimmerman (1971). This was true at the time of the sedimentation of the detrital components. Carbonate-cemented deposits, however, experience accumulation (and sometimes dissolution) of carbonate as a pore-filling substance over time (Nathan and Mauz, 2008). As this interstitial cement material is inert, the dose rate of carbonate-rich sediments should be corrected in a similar manner to water, but with new correction factors after the pore material stops changing, the carbonate has already precipitated in the existing pore and the changing has ceased (Nathan and Mauz, 2008; Mauz and Hoffmann, 2014; Erginal et al., 2021). Thus, the dose rate is not constant during burial, indicating higher values at the time of sedimentation of the detrital components and lower values after cementation. Table 3, besides the conventional values of dose rates and ages, also includes the effective dose rate and the final ages.

The calculated ages are very old, in many cases beyond the usually reported dating results of 400–500 ka, considering both the large values of the equivalent doses but mostly the low dose rate in the carbonate rocks and sediments. However, these conversion factors do not take account of spatial heterogeneities in sediments such as restricted radioactive source geometries, where the grain size and source density are significant for accurate beta dose rate calculation (Guerin et al., 2012). The calculation assumes the infinite matrix approach that is justified in pottery, as in many cases the quartz grains are surrounded by a quasi-infinite, uniform medium. Of course, even for these cases, the inhomogeneity of the various elements' content results in severe dose rate in-homogeneity; as the example in (Aidona et al., 2018) shows. However, in contexts such as carbonate cemented aeolianites, sedimentary grains are not surrounded by either an infinite or uniform matrix. According to Monte Carlo simulations (Guerin et al., 2012, 2015) for the specific grain size fraction, the dose rate in quartz could be underestimated by factors ranging from 15% to 40%. Regardless, the dose rates that were calculated in previous studies of Şile aeolianites (Polymeris et al., 2012; Erginal et al., 2013, 2017) are in good agreement with those of the present study.

4. Discussion

4.1. A general outline of aeolianite ages on world coasts

Although OSL age distributions show a very wide time interval, this is normal because of the dynamic structure of the aeolian systems, and the permanent stability of the dune sands depends on cementing rather than vegetation. As a matter of fact, despite the most common period of aeolianite formation being MIS 5, which is the last warm interglacial period (Kindler and Hearty, 1995; Carew and Mylroie, 1997; Sivan et al., 1999; Hearty and Neumann, 2001; Hearty, 2002, 2003; Mylroie, 2008; Carr et al., 2010; Erginal et al., 2013), there are many records pinpointing aeolianite occurrences from Holocene to Middle Quaternary, such as those on Majorca Island in the Western Mediterranean (34–97 ka, Fornos et al., 2009), on the northwest coast of Egypt (191–584 ka, El-Asmar and Wood, 2000), in South Africa (67–366 ka, Bateman et al., 2004; Porat and Botha, 2008), in Australia (10–533 ka, Gardner et al., 2006; Hearty and O'Leary, 2008; Brooke et al., 2014; Lipar and Webb, 2014), on the coast of Israel (Holocene-MIS 7.1, Sivan et al., 1999;

Table 3
OSL ages of aeolianite (E) and paleosol (SP) samples.

Lab Code	Depth (cm)	U content (ppm)	Th content (ppm)	$CaCO_3$ content (%)	K content (%)	De (Gy)	σDe (Gy)	DR_{conv} (Gy/ka)	$σDR_{conv}$ (Gy/ka)	Age_{conv} (ka)	$σAge_{conv}$ (ka)	DR_{eff} (Gy/ka)	$σDR_{eff}$ (Gy/ka)	Age_{corr} (ka)	$σAge_{corr}$ (Gy/ka)	MIS period
E-6.1	850	0.1	1.1	69,0	0.01	140.17	4.7	0.18	0.02	773	104	0.21	0.03	668	111	Pre-15
E-6.2	800	0.1	1.7	75	0.01	152.75	4.07	0.21	0.02	743	85	0.24	0.03	632	88	Pre-15
E-3.1	280	0.1	1	69.5	0.01	151.38	3.24	0.24	0.02	637	67	0.28	0.02	547	69	15–14
E-6.3	750	0.1	1	72	0.02	116.5	2.1	0.19	0.02	616	77	0.22	0.03	528	81	15–14
E-5.1	390	0.1	0.9	81,0	0.01	133.97	3.47	0.22	0.02	622	68	0.26	0.03	522	73	15–14
E-6.4	700	0.1	0.7	83	0.01	105.18	3.95	0.17	0.02	606	80	0.21	0.03	507	84	15–14
E-4.1	280	0.1	0.9	68.1	0.02	121.35	2.29	0.23	0.03	538	79	0.26	0.03	465	82	13–12
E-2.2	250	0.1	0.6	81.8	0.02	117.07	3.55	0.23	0.02	504	53	0.28	0.03	427	56	13–12
E-2.1	280	0.1	0.6	81.4	0.02	114.98	4.59	0.23	0.02	504	55	0.27	0.03	423	59	13–12
E-3.2	190	0.1	0.7	79.9	0.01	115.99	3.38	0.24	0.02	489	50	0.28	0.03	411	53	13–12
E-7.1	280	0.2	1.1	86.8	0.01	130.31	4.77	0.25	0	525	51	0.3	0.03	436	53	13–12
E-5.2	230	0.1	0.7	88.7	0.01	123.05	6.47	0.24	0.02	519	56	0.29	0.03	428	61	13–12
P2	500	0.3	3	16,4	0.03	182,66	7,85	0,42	0,04	444	42	0,44	0,05	426	48	12–11
E-2.3	220	0.1	0.8	77.8	0.01	114.43	3.38	0.24	0.02	477	49	0.29	0.03	404	54	11–10
E-5.3	130	0.1	1.3	84.8	0.02	125.88	7.29	0.28	0.02	447	45	0.34	0.04	372	49	11–10
E-1.1	300	0.1	0.8	76.8	0.02	99.61	3.9	0.23	0.02	433	47	0.27	0.03	367	55	11–10
E-3.3	120	0.1	0.9	85.8	0.02	119	5.46	0.28	0.03	430	52	0.33	0.03	357	55	11–10
E-7.2	180	0.2	1	82.5	0.02	112.7	3.47	0.27	0.02	422	39	0.32	0.03	354	44	11–10
E-1.2	250	0.1	0.6	87.6	0.02	99.71	2.31	0.24	0.02	424	42	0.28	0.03	351	49	11–10
E-7.3	30	0.2	1.1	84.3	0.01	135.38	6.47	0.35	0.03	386	40	0.42	0.04	322	47	9–8
E-1.3	50	0.1	0.8	76.6	0.02	109.8	1.42	0.3	0.03	360	30	0.36	0.04	305	37	9–8
E-2.4	180	0.1	0.7	75.6	0.01	79.92	2.54	0.24	0.02	329	34	0.29	0.03	280	44	9–8
P1	100	0.3	5.2	10,3	0.01	194,45	9,16	0,70	0,04	278	20	0,73	0,04	267	22	8–7

Frechen et al., 2002, 2004; Sivan and Porat, 2004) and in Bermuda and the Bahamas (MIS 5 - MIS 11, Brooke, 2001). A significant number of these aeolianite formation stages coincides with interglacial periods.

When aeolianite formation is considered for the last 800 ka, the warmest interglacial periods are MIS 5.5 and 11, while the coldest interglacial periods are MIS 13 and 17. In terms of glacial periods, the coldest periods are MIS 2, 12 and 16, while the hottest glacial period is MIS 14 (Masson-Delmotte et al., 2010). MIS 11 is considered to be the longest and warmest interglacial period in Pleistocene (Rousseau et al., 1992; Oppo et al., 1990; Howard and Prell, 1992). MIS 14, when abnormally warm and humid conditions were experienced, merged with the cooler MIS 13 and MIS 15 before the Mid-Brunhes event caused the formation of a "plateau-like" super interglacial phase (Yu and Chen, 2011). MIS 13 is a phase that encountered strong summer monsoons in the northern hemisphere. During this stage, there were important changes in grain size distribution in the loess deposits on the loess plateau of China (Vandenberghe et al., 1997).

4.2. Formation stages of Şile aeolianites

4.2.1. The earliest stage of aeolianite formation

When the paleoclimate conditions described above are evaluated in terms of the obtained OSL ages, the ages obtained from the lowest levels of the section with a maximum apparent thickness of 8 m are 668 ± 111 thousand years and 632 ± 88 thousand years. Considering the margins of error, these results reflect an age of at least MIS 15 but earlier than MIS 17 for the accumulation of calcium carbonates with the first aeolianite (quartz) sands. These ancient aeolianites, corresponding to Middle Pleistocene, rest on a reddish brown paleosol level.

The paleosol under the aeolianite was formed on Eocene-aged hardened sandy silts and explains how decomposition occurred under highly humid conditions prior to the precipitation of the aeolianite sands. XRD analysis of the samples taken from the paleosol showed 99.8% quartz and 0.2% calcite. Calcium carbonate and total organic carbon are 0% and 0.65%, respectively. The Rb / Sr ratio calculated from the results of ICP-MS analysis of the samples is 0.76, which is evidence that the soil was strongly washed. Accordingly, the first aeolian activity must have started in a sharp dry-windy phase following these very conditions. In the first aeolianite layers overlying this paleosol, the quartz rate varies between 88.4 and 84.1%, the calcite ratio is between 15.9 and 14.6%, and the Sr rate varies between 92 and 114 ppm, which is much higher than the lower paleosol, containing 15 ppm Sr.

This period, which corresponds to the beginning of Middle Pleistocene, includes the Brunhes-Matuyama magnetic polarity reversal phase, defined as a distinct polarity reversal, which is assumed to have occurred at 780 ka (Shackleton et al., 1990), 775 ka BP (Bassinot et al., 1994), or 777.6 ka (Hyodo and Kitaba, 2015). Albeit not recognized at the bottom of the aeolianite section, our measurements demonstrated that the studied aeolianite unit was deposited during normal polarity, Brunhes chron, and is not older than 780 ka. These results also match well with the OSL dating, which was found to be around 700 ka at the bottom part of the aeolianite unit.

This transition period from Lower Pleistocene to Middle Pleistocene represents the transition to dry conditions in Australia (Pillans, 2003). The correct chronostratigraphy of this reversal transition phase is very problematic compared with the studies conducted in loess sediments in China and the loess-paleosol sequences in the northern coastal belt of the Black Sea, where more climatic cycles occurred after this phase than before (Dodonov et al., 2006). In fact, this phase represents the most important climatic change in the Early-Middle Pleistocene transition (Head and Gibbard, 2005). The formation of the paleosol, located under the first layers of aeolianite in the study area, is evidence of the moist conditions in this transition phase. Following this transition phase, MIS 19 should be climatically drier, an interglacial period in which carbonate precipitation is effective and there is a connection with the Mediterranean. There is no other explanation for the composition and

origin of the aeolianites, which are of an ooidic sandstone structure, containing more than 85% calcium carbonate and almost similar to the Bahamian carbonate aeolianites.

4.2.2. MIS 15–14

The OSL ages of four samples yielded age values ranging from 547 ± 69 ka to 507 ± 84 ka, the Early Middle Pleistocene. Aeolian activity might have increased during the transition period from MIS 15 to MIS 14. Suggestive of increasing aridity that favours aeolian wind-blown sand drift, the calcite ratio in the samples reaches 78.5% and the carbonate content is 76% on average. It can be suggested that, following this transition phase, precipitation of connective carbonates of aeolianite occurred during the warmer climatic conditions of MIS 15.

4.2.3. MIS 13–12 transition

The OSL ages of six aeolianite samples, ranging from 465 ± 82 ka to 411 ± 53 ka, point to the interglacial conditions prior to the MIS 13–12 transition and the Mid-Brunhes event (MBE), after a long period when aeolianite sands did not accumulate during the ice age of MIS 14 after MIS 15. The amount of $CaCO_3$ is about 89% higher than the previous (MIS 16–15) aeolianite formation stage. According to XRD analysis, the calcite average is 77.2% and the quartz average is 22.5%. Results from loess depots in China (Vandenberghe, 2000; Sun et al., 2006; Guo et al., 2009), data from the lower reaches of the River Danube (Fitzsimmons et al., 2012), and even research results from Siberia during MIS 13 all indicate that relatively warm climatic conditions prevailed and glacial volumes decreased globally. The core samples taken from Lion Bay in the south of France showed that warm conditions were dominant in the next interglacial stages (Cortina et al., 2016). Therefore, in MIS 13–12, carbonates carried from the shelf environment that were exposed in the transition phase from interglacial to glacial conditions support a cementing process taking place in the increasingly windy arid conditions, resulting in aeolianite formation.

4.2.4. MIS 11–10 transition

The OSL ages of six aeolianite samples yielded ages ranging between 404 ± 54 ka and 351 ± 49 ka. This period must be the transition phase from the MIS 11 interglacial age to the MIS 10 ice age and coincides with the period immediately after the Mid-Brunhes event (MBE). As is known, the Mid-Brunhes incident is considered to be a global climate variance caused by orbital change during the transition from MIS 12 to 11 (Termination V) about 430,000 years ago. Terrestrial and marine records show that after this period, glacial conditions were dominant in the northern hemisphere in contrast to the southern hemisphere, which was dominated by interglacial conditions (Jansen et al., 1986).

In the MIS 12 ice age, the sea level that had dropped −130 m (Shackleton, 1987) rose in MIS 11, known as the hottest and longest-lasting interglacial of the last 500,000 years (McManus et al., 2003; Bowen, 2010). During the MIS 11 interglacial, which is longer than MIS 5e and is considered an analogue of the future of the (Holocene) climate (Rohling et al., 2010), the glacier volumes were less than in the present-day glacial phase (Bauch et al., 2000), and the sea level was higher than today (for example, in Bermuda and the Bahamas; Hearty et al., 1999; Hearty and Olson, 2008; Olson and Hearty, 2009).

In the aeolianites where the $CaCO_3$ ratios are 85%, XRD analysis showed the presence of 84.5–75.4% calcite and 15.5–24.6% quartz. As with the other aeolianites, the precipitation of the carbonate cement in the aeolianites occurred in hot and dry conditions during the MIS 11 interglacial period.

4.2.5. MIS 9–8 transition

OSL ages of four samples ranging from 322 ± 47 ka to 280 ± 44 ka probably correspond to the transition period from MIS 9 to MIS 8, in which the maximum sea level rise is experienced during the MIS 9c phase (Siddall et al., 2006). Regarding the MIS 9 period, which is under-recognized in comparison with the MIS 5, MIS 7 and MIS 11 interglacials, the rising corals on Henderson Island in the South Pacific have yielded ages between 334 ± 4 ka and 306 ± 4 ka based on U/Th data (Stirling et al., 2001). In this period, the sea level is assumed to be approximately today's sea level in southern Australia (Murray-Wallace, 2002), Bermuda and the Bahamas (Hearty and Kindler, 1995), and Grand Cayman (Vezina et al., 1999).

The aeolianites of this period contain $CaCO_3$ varying between 75% and 87%, similar to that of MIS 11–10. Calcite and quartz are 78.3% and 21.7%, respectively. Evidence of MIS 9 stages on the coast of Turkey is very limited. The results of ESR dating of fossilised shells containing bivalve species such as *Chione* sp. gave an age of 292.5 ± 49.8 ka (Keskin and Pedoja, 2011).

4.2.6. Paleosol formation periods

The OSL age of paleosol P1 is 267 ± 22 ka. This period must have been a short-term moist-rainy phase in which aeolianite formation changes from windy and arid conditions to more humid and rainy conditions. The period corresponds to a short-term soil formation phase in the transition period (Termination III) between phases MIS 8b and MIS 7e according to the oxygen isotope chronology.

The age of P2 paleosol is 426 ± 48 ka and this period should correspond to the MIS 12-MIS 11 transition (Termination V; Middle Brunhes Event) according to the oxygen isotope chronology. In this sample, the presence of 8.6% lithium zeolite as hydrated aluminium silicate is interesting. Since natural zeolite formation depends on the chemical reaction that occurs as a result of the contact between saline water with high pH and volcanic tuffs, its presence in the studied aeolianites is not in situ filling. In fact, in aeolianites where paleosols developed, no zeolite has been identified in the XRD analysis. Therefore, the source of the abundant lithium zeolite contained in the paleosols may either be associated with volcanic activity synchronized with the formation of the soil or transport from Upper Cretaceous volcanics (Esenli et al., 1997) in the Kocaeli Peninsula.

5. Conclusions

The migrating and climbing transverse dune and interdune system (flat sand sheets) comprising the Şile aeolianite provides a new and robust record for the determination of five Mediterranean transgressions of the Black Sea during the interglacials before MIS 5. After the Messinian event, in which well-sorted oolithic calcarenites were also deposited, ooids were first identified in these Middle Quaternary aeolian dunes. Following the transition period from Lower Pleistocene to Middle Pleistocene, the initial formation of aeolianite occurred during MIS 19 when the Black Sea was connected with the Mediterranean. In other words, the onset of aeolian deposition and the following cementation occurred at normal polarity chron, preserving normal polarity and with no layers in reverse. This also explains why the MIS 19 interglacial did not start immediately after the Brunhes-Matuyama magnetic reversal phase. During MIS 15, 13, 11 and 9 interglacials dominated by effective carbonate precipitation due to climatically warmer and drier conditions, the connective carbonates and ooids precipitated from evaporated sea water. The transportation of sands and carbonates to the coastal sand dunes, together with the ooids, by onshore winds occurred due to the lowering of the sea level. Paleosols, on the other hand, witness the intervening soil formation periods during the relatively rainy Termination III and V.

Declaration of Competing Interest

The authors declare that they have no known competing financial interests or personal relationships that could have appeared to influence the work reported in this paper.

Acknowledgements

This work was supported by the Scientific and Technological Research Council of Turkey (TUBITAK; project number: 113Y418) and the Turkish Academy of Sciences (TUBA). We would like to thank Mustafa Avcıoğlu, Çağlar Çakır, Emrah Özpolat, Hakan Kaya and Abdullah Akbaş for their assistance in the field studies. Graham Lee is thanked for his help in correcting the English text of the article. We are honoured to dedicate this study in loving memory of the great Turkish Geographer, Professor Oğuz Erol, who passed away on April 11, 2014.

Appendix A. Supplementary data

Supplementary data to this article can be found online at https://doi.org/10.1016/j.palaeo.2022.110902.

References

Abegg, F.E., Loope, D., Harris, P.M., 2001. Carbonate eolianites: Depositional models and diagenesis. In: Abegg, F.E., Harris, P.M., Loope, D.B. (Eds.), Modern and Ancient Carbonate Eolianites: Sedimentology, Sequence Stratigraphy, and Diagenesis, 71. SEPM Special Publication, pp. 17–30.
Aidona, E., Polymeris, G.S., Camps, P., Kondopoulou, D., Ioannidis, N., Raptis, K., 2018. Archaeomagnetic versus luminescence methods: the case of an early byzantine ceramic workshop in Thessaloniki, Greece. Archaeol. Anthropol. Sci. 2018 (10), 725–741.
Arslanov, Kh.A., 1993. Late pleistocene geochronology of European Russia. Radiocarbon. 35 (3), 421–427.
Badertscher, S., Fleitmann, D., Cheng, H., Edwards, R.L., Göktürk, O.M., Zumbühl, A., Leuenberger, M., Tüysüz, O., 2011. Pleistocene water intrusions from the Mediterranean and Caspian seas into the Black Sea. Nat. Geosci. 4 (4), 236–239.
Banerjee, D., Bøtter-Jensen, L., Murray, A.S., 1999. Retrospective Dosimetry: preliminary use of the single aliquot regeneration (SAR) protocol for the measurement of quartz dose in young house bricks. Radiat. Prot. Dosim. 84, 421–426.
Banerjee, D., Murray, A.S., Bøtter Jensen, L., Lang, A., 2001. Equivalent dose estimation using a single aliquot of polymineral fine grains. Radiat. Meas. 33, 73–94.
Bassinot, F.C., Labeyrie, L.D., Vincent, E., Quidelleur, X., Shackleton, N.J., Lancelot, Y., 1994. The astronomical theory of climate and the age of the Brunhes-Matuyama magnetic reversal. Earth Planet Sci. Lett. 126 (1–3), 91–108.
Bateman, M.D., Holmes, P.J., Carr, A.S., Horton, B.P., Jaiswal, M.K., 2004. Aeolianite and barrier dune construction spanning the last two glacial–interglacial cycles from the southern Cape coast, South Africa. Quat. Sci. Rev. 23, 1681–1698.
Bauch, H.A., Erlenkeuser, H., Helmke, J.P., Struck, U., 2000. A paleoclimatic evaluation of marine oxygen isotope stage 11 in the high-northern Atlantic (Nordic Seas). Glob. Planet. Chang. 24, 27–39.
Bigarella, J.J., 1972. Eolian environments: their characteristics, recognition and importance. In: Rigby, J.K., Hamblin, H.K. (Eds.), Recognition of Ancient Sedimentary Environments: Soc. Econ. Paleontologists and Mineralogists Spec. Pub, 16, pp. 12–62.
Bøtter-Jensen, L., 1997. Luminescence techniques: instrumentation and methods. Radiat. Meas. 17, 749–768.
Bøtter-Jensen, L., Bulur, E., Duller, G.A.T., Murray, A.S., 2000. Advances in luminescence instrument systems. Radiat. Meas. 32, 523–528.
Bowen, D.Q., 2010. Sea level ~400 000 years ago (MIS 11): Analogue for present and future sea-level? Clim. Past 6 (1), 19–29.
Bristow, C., Mountney, N.P., 2013. Aeolian landscapes, aeolian stratigraphy. In: Shroder, J.F. (Ed.), Treatise on Geomorphology. Elsevier, Nova York, pp. 246–268.
Brooke, B.P., 2001. The distribution of carbonate eolianite. Earth Sci. Rev. 55 (1–2), 135–164.
Brooke, B.P., Murray-Wallace, C.V., Woodroffe, C.D., Heijnis, H., 2003. Quaternary aminostratigraphy of eolianite on Lord Howe Island, Southwest Pacific Ocean. Quat. Sci. Rev. 22 (2–4), 387–406.
Brooke, B.P., Olley, J.M., Pietsch, T., Playford, P.E., Haines, P.W., Murray-Wallace, C.V., Woodroffe, C.D., 2014. Chronology of Quaternary coastal aeolianite deposition and the drowned shorelines of southwestern Western Australia - a reappraisal. Quat. Sci. Rev. 93, 106–124.
Butzer, K.W., 2004. Coastal eolian sands, paleosols, and Pleistocene geoarchaeology of the Southwestern Cape, South Africa. J. Archaeol. Sci. 31 (12), 1743–1781.
Carew, L., Mylroie, J.E., 1997. Geology of the Bahamas, (eds. Vacher, H.L., Quinn, T.) geology and hydrogeology of carbonate islands. Dev. Sedimentol. 54, 91–139.
Carew, J.L., Mylroie, J.E., 2001. In: Abegg, F.E., Harris, P.M., Loope, D.B. (Eds.), Quaternary Carbonate Eolianites of the Bahamas: Useful Analogues for the Interpretation of Ancient Rocks? Modern and Ancient Carbonate Eolianites: Sedimentology, Sequence Stratigraphy, and Diagenesis, 71. SEPM Special Publication.
Carr, A.S., Bateman, M.D., Roberts, D.L., Murray-Wallace, C.V., Jacobs, Z., Holmes, P.J., 2010. The last interglacial sea-level high stand on the southern Cape coastline of South Africa. Quat. Res. 73, 351–363.
Chen, J., An, Z., Head, J., 1999. Variation of Rb/Sr ratios in the Loess-Paleosol sequences of central China during the last 130,000 years and their implications for monsoon paleoclimatology. Quat. Res. 51, 215–219.
Cortina, A., Grimalt, J.O., Martrat, B., Rigual-Hernández, A., Sierro, F.J., Flores, J.A., 2016. Anomalous SST warming during MIS 13 in the Gulf of Lions (Northwestern Mediterranean Sea). Org. Geochem. 92, 16–23.
Daly, R.A., 1925. Pleistocene changes of level. Am. J. Sci. 10, 281–313.
Dirks, et al., 2010. Geological setting and Age of Australopithecus sediba from Southern Africa. Science 328, 205–208.
Dodonov, A.E., Zhou, L.P., Markova, A.K., Tchepalyga, A.L., Trubikhin, V.M., Aleksandrovski, A.L., Simakova, A.N., 2006. Middle-Upper Pleistocene bioclimatic and magnetic records of the Northern Black Sea Coastal area. Quat. Int. 149, 44–54.
El-Asmar, H.M., Wood, P., 2000. Quaternary shoreline development: the northwestern coast of Egypt. Quat. Sci. Rev. 19 (11), 1137–1149.
Engelmann, A., Neber, A., Frechen, M., Boenigk, W., Ronen, A., 2001. Luminescence chronology of upper pleistocene and holocene aeolianites from Netaya South—Sharon Coastal Plain, Israel. Quatern. Sci. Rev. 20, 799–804.
Erginal, A.E., Kiyak, N.G., Ekinci, Y.L., Demirci, A., Ertek, A., Canel, T., 2013. Age, composition and paleoenvironmental significance of a late Pleistocene eolianite from the western Black Sea coast of Turkey. Quat. Int. 296, 168–175.
Erginal, A.E., Kıyak, N.G., Öztürk, M.Z., Selim, H.H., Ekinci, Y.L., Demirci, A., Kırcı Elmas, E., Öztürk, T., Çakır, Ç., Karabıyıkoğlu, M., 2017. Eolianite and coquinite as evidence of MIS 6 and 5, NW Black Sea Coast, Turkey. Aeolian Res. 25, 1–9.
Erginal, A.E., Polymeris, G.S., Erenoğlu, O., Giannoulatou, V., Meriç, E., Karataş, A., Şahiner, E., Selim, H.H., 2021. New record of calcarenite in Hatay, Turkey: an evidence of the Late Pleistocene Eastern Mediterranean–Red Sea connection. Arab. J. Geosci. 14, 2104.
Esenli, F., Uz, B., Kumbasar, I., 1997. Mordenite type zeolite occurrence in the Upper cretaceous volcanics of Şile region, İstanbul-Turkey. Geol. Bull. Turkey. 40, 43–49.
Fairbridge, R.W., Johnson, D.L., 1978. Eolianite. In: Fairbridge, R.W., Bourgeois, J.Ž. (Eds.), The Encyclopedia of Sedimentology. Dowden, Hutchinson and Ross, Stroudsburg, PA, pp. 279–282.
Fedorov, P.V., 1978. Pleistotsen Ponto-Kaspiya, Nauka, Moscow.
Fisher, R.A., 1953. Dispersion on a sphere. P R Soc. Lond. A217, 295–305.
Fitzsimmons, K.E., Marković, S.B., Hambach, U., 2012. Pleistocene environmental dynamics recorded in the loess of the middle and lower Danube basin. Quat. Sci. Rev. 41, 104–118.
Fletcher, C.H., Murray-Wallace, C.V., Glenn, C.R., Shermanc, C.E., Popp, B., Hessler, A., 2005. Age and origin of late quaternary eolianite, Kaiehu point (Moornomi), Molokai, Hawaii. J. Coast. Res. 42, 97–112.
Foos, A.M., 1991. Aluminous lateritic soils, Eleuthera, Bahamas: a modem analog to carbonate paleosols. J. Sediment. Petrol. 61, 340–348.
Fornos, J.J., Clemmensen, L.B., Gomez-Pujol, L., Murray, A.S., 2009. Late Pleistocene carbonate aeolianites on Mallorca, Western Mediterranean: a luminescence chronology. Quat. Sci. Rev. 28, 2697–2709.
Frébourg, G., Hasler, C.A., Davaus, E., 2010. Catastrophic event recorded among Holocene eolianites (Sidi Salem formation, SE Tunisia). Sediment. Geol. 224 (1–4), 38–48.
Frechen, M., Dermann, B., Boenigk, W., Ronen, A., 2001. Luminescence chronology of aeolianites from the section at Givat Olga—Coastal Plain of Israel. Quat. Sci. Rev. 20, 805–809.
Frechen, M., Neber, A., Dermann, B., Tsatskin, A., Boenigk, W., Ronen, A., 2002. Chronostratigraphy of aeolianites from the Sharon Coastal Plain of Israel. Quat. Int. 89 (1), 31–44.
Frechen, M., Neber, A., Tsatskin, A., Boenigk, W., Ronen, A., 2004. Chronology of Pleistocene sedimentary cycles in the Carmel Coastal Plain of Israel. Quat. Int. 121 (1), 41–52.
Fryberger, S.G., 1979. Dune forms and wind regimes. In: McKee, E.D. (Ed.), A Study of Global Sand Seas. United States Geological Survey, Professional Paper. U.S.G.S. Professional Paper, pp. 137–140.
Fryberger, S.G., Schenk, C.J., 1988. Pin-stripe lamination: a distinctive feature of modern and ancient aeolian sediments. Sediment. Geol. 55, 1–15.
Fumanal, M.P., 1995. Pleistocene dune systems in the Valencian Betic cliffs ŽSpain.. INQUA Subcomission on Mediterranean and Black Sea Shorelines. Newsletter 17, 32–38.
Gardner, T.W., Webb, J., Davis, A.G., Cassel, E.J., Pezzia, C., Merritts, D.J., Smith, B., 2006. Late Pleistocene landscape response to climate change: eolian and alluvial fan deposition, Cape Liptrap, southeastern Australia. Quat. Sci. Rev. 25, 1552–1569.
Gillet, H., Lericolais, G., Réhault, J.P., 2007. Messinian event in the Black Sea: evidence of a Messinian erosional surface. Mar. Geol. 244, 142–165.
Guerin, G., Mercier, N., Nathan, R., Adamiec, G., Lefrais, Y., 2012. On the use of the infinite matrix assumption and associated concepts: a critical review. Radiat. Meas. 47, 778–785.
Guerin, G., Jain, M., Thomsen, K., Murray, A.S., Mercier, N., 2015. Modelling dose rate to single grains of quartz in well-sorted sand samples: the dispersion arising from the presence of potassium feldspars and implications for single grain OSL dating. Quat. Geochronol. 27 (2015), 52–65.
Guo, Z.T., Berger, A., Yin, Q.Z., Qin, L., 2009. Strong asymmetry of hemispheric climates during MIS-13 inferred from correlating China loess and Antarctica ice records. Clim. Past 5 (1), 21–31.
Head, M.J., Gibbard, P.L., 2005. Early–Middle Pleistocene transitions: an overview and recommendation for the defining boundary. In: Head, M.J., Gibbard, P.L. (Eds.), Early–Middle Pleistocene Transitions: the Land–Ocean Evidence, 247. Bath. Geol Soc Spec Publ, pp. 1–18.
Hearty, P.J., 2002. Revision of the late Pleistocene stratigraphy of Bermuda. Sediment. Geol. 153, 1–21.
Hearty, P.J., 2003. Stratigraphy and timing of eolianite deposition on Rottnest Island, Western Australia. Quat. Res. 60, 211–222.

Hearty, P.J., Kindler, P., 1995. Sea level highstand chronology from stable carbonate platforms (Bermuda and the Bahamas). J. Coast. Res. 11 (3), 675–689.
Hearty, P.J., Neumann, A.C., 2001. Rapid sea level and climate change at the close of the last Interglaciation (MIS 5e): evidence from the Bahama Islands. Quat. Sci. Rev. 20, 1881–1895.
Hearty, P.J., O'Leary, M.J., 2008. Carbonate eolianites, quartz sands, and Quaternary Sea-level cycles, Western Australia: a chronostratigraphic approach. Quat. Geochronol. 3 (1–2), 26–55.
Hearty, P.J., Olson, S.L., 2008. Mega-highstand or megatsunami? Discussion of McMurtry et al., Elevated marine deposits in Bermuda record a late Quaternary megatsunami. Sediment. Geol. 203 (3–4), 307–312.
Hearty, P.J., Vacher, H.L., 1994. Quaternary stratigraphy of Bermuda: a high-resolution pre-Sangamonian rock record. Quat. Sci. Rev. 13 (8), 685–697.
Hearty, P.J., Kindler, P., 1997. The stratigraphy and surficial geology of New Providence and surrounding islands, Bahamas. J. Coastal Res. 13, 798–812.
Hearty, P.J., Kindler, P., Cheng, H., Edwards, R.L., 1999. A +20 m middle Pleistocene Sea-level highstand (Bermuda and the Bahamas) due to partial collapse of Antarctic ice. Geology. 27 (4), 375–378.
Herwitz, S., Muhs, D.R., Prospero, J., Mahan, S., Vaughn, B., 1996. Origin of Bermuda's clayrich Quaternary paleosols and their paleoclimatic significance. J. Geophys. Res.-Atmos. 101 (D18), 23389–23400.
Howard, W.R., Prell, W.L., 1992. Late Quaternary surface circulation of the Southern Indian Ocean and its relationship to orbital variations. Paleoceanography. 7, 79–117.
Hsü, K.J., Giovanoli, F., 1979. Messinian event in the Black Sea. Palaeogeogr. Palaeocl. 29, 75–93.
Hunter, R.E., 1977. Basic types of stratification in small eolian dunes. Sedimentology. 24, 361–388.
Huntley, D.J., 1985. On the zeroing of the thermoluminescence of sediments. Phys. Chem. Miner. 12, 122–127.
Hyodo, M., Kitaba, I., 2015. Timing of the Matuyama–Brunhes geomagnetic reversal: Decoupled thermal maximum and sea-level highstand during Marine Isotope Stage 19. Quat. Int. 383, 136–144.
Jansen, J.H.F., Kuijpers, A., Troelstra, S.R., 1986. A Mid-Brunhes climatic event: long-term changes in global atmosphere and ocean circulation. Science. 232, 619–622.
Kalafat, D., 2017. Seismicity and tectonics of the Black Sea. Int. J. Earth Sci. Geophys. 3, 011.
Kendrick, G.W., Wyrwoll, K.H., Szabo, B.J., 1991. Pliocene– Pleistocene coastal events and history along the western margin of Australia. Quat. Sci. Revi. 10, 419–439.
Keskin, S., Pedoja, K., Bektas, O., 2011. Coastal uplift along the eastern Black Sea coast: new marine terrace data from Eastern Pontides, Trabzon (Turkey) and a Review. J. Coast. Res. 27, 63–73.
Kindler, P., Hearty, P.J., 1995. Pre-Sangamonian eolianites in the Bahamas? New evidence from Eleuthera Island. Mar. Geol. 127 (1–4), 73–86.
Kirschvink, L., 1980. The least-squares line and plane and the analysis of palaeomagnetic data. Geophys. J. Roy. Astr. Soc. 62, 699–718.
Kitis, G., Kiyak, N.G., Polymeris, G.S., 2015. Temperature lags of luminescence measurements in a commercial luminescence reader. Nucl. Instrum. Methods Phys. Res. Sect. B Beam. Interact. Mater. Atoms. 359, 60–63.
Kocurek, G., Dott, R.H., 1981. Distinction and uses of stratification types in the interpretation of eolian sand. J. Sediment. Petrol. 51, 579–595.
Lancaster, N., Teller, J.T., 1988. Interdune deposits of the Namib Sand Sea. Sediment. Geol. 55, 91–107.
Li, S.-H., Li, B., 2019. TL/OSL Dating (Chapter 10) in: Advances in Physics and Applications of Optically and Thermally Stimulated Luminescence, World Scientific by Reuven Chen and Vasilis Pagonis.
Lian, O.B., Hu, J., Huntley, D.J., Hicock, S.R., 1995. Optical dating studies of quaternary organic–rich sediments from southwestern British Columbia and northwestern Washington State. Can. J. Earth Sci. 32, 1194–1207.
Lipar, M., Webb, J.A., 2014. Middlelate Pleistocene and Holocene chronostratigraphy and climate history of the Tamala Limestone, Cooloongup and Safety Bay Sands, Nambung National Park, southwestern Western Australia. Aust. J. Earth Sci. 61, 1023–1039.
Liritzis, I., Singhvi, A.K., Feathers, J.K., Wagner, G.A., Kadereit, A., Zacharias, N., Li, S.-H., 2013a. Luminescence Dating in Archaeology, Anthropology and Geoarchaeology: An Overview (Springer Briefs in Earth System Sciences). https://doi.org/10.1007/978-3-319-00170-8.pdf.
Liritzis, I., Stamoulis, K., Papachristodoulou, C., Ioannides, K., 2013b. A reevaluation of radiation dose rate conversion factors. Mediterr. Arch. Archaeomet. 13 (3), 1–15.
Lowrie, W., 1990. Identification of ferromagnetic minerals in a rock by coercivity and unblocking temperature properties. Geophys. Res. Lett. 17, 159–162.
Masson-Delmotte, V., Stenni, B., Pol, K., Braconnot, P., Cattani, O., Falourd, S., Kageyama, M., Jouzel, J., Landais, A., Minster, B., Krinner, G., Johnsen, S., Röthlisberger, R., Chappellaz, J., Hansen, J., Mikolajewicz, U., Otto-Bliesner, B., 2010. EPICA Dome C record of glacial and interglacial intensities. Quat. Sci. Rev. 29 (1–2), 113–128.
Mauz, B., Hoffmann, D., 2014. What to do when carbonate replaced water: Carb, the model for estimating the dose rate of carbonate-rich samples. Ancient TL 32 (2), 24–32.
McKee, E.D., Bigarella, J.J., 1972. Deformational structures in Brazillian coastal dunes. J. Sediment. Res. 42, 670–681.
McManus, J.F., Oppo, D.W., Cullen, J., Healey, S., 2003. In: Droxler, A.W., Poore, R.Z., Burckle, L.H. (Eds.), Marine Isotope Stage 11 (MIS 11): Analog for Holocene and Future Climate? Earth's Climate and Orbital Eccentricity: The Marine Isotope Stage 11 Question. Wiley, Washington.
Muhs, D.R., Skipp, G., Schumann, R.R., Johnson, D.L., McGeehin, J.P., Beann, J., Freeman, J., Pearce, T.A., Rowland, Z.M., 2009. The origin and paleoclimatic significance of carbonate sand dunes deposited on the California Channel Islands during the last glacial period. In: Damiani, C.C., Garcelon, D.K. (Eds.), Proceedings of the 7th California Islands Symposium. Institute for Wildlife Studies, Arcata-California.
Muhs, D.R., Budahn, J.R., Prospero, J.M., Skipp, G., Herwitz, S.R., 2012. Soil genesis on the Island of Bermuda in the quaternary: the importance of African Dust transport and deposition. J. Geophys. Res. Earth. 117 (F3), 1–20.
Murray, A.S., Wintle, A.G., 2000. Luminescence dating of quartz using an improved single-aliquot regenerative-dose protocol. Radiat. Meas. 32, 57–73.
Murray, A.S., Wintle, A.G., 2003. The single aliquot regenerative dose protocol: potential for improvements in reliability. Radiat. Meas. 37, 377–381.
Muhs, D.R., Whelan, J.F., Kennedy, G.L., Rockwell, T.K., 1993. Late Quaternary sea level history of the pacific coast of North America: a detailed record of the Last GlacialrInterglacial cycle. In: Kelmelis, J.A., Snow, M.Ż. (Eds.), US Geological Survey Global Change Research Forum. US Geological Survey, Herndon, VA, pp. 101–102.
Murray, A.S., Buylaert, J.P., Thiel, C., 2015. A luminescence dating intercomparison based on a Danish beach-ridge sand. Radiat. Meas. 81, 32–38.
Murray-Wallace, C.V., 2002. Pleistocene coastal stratigraphy, sea level highstands and neotectonism of the southern Australian passive continental margin – a review. J. Quat. Sci. 17 (5–6), 469–489.
Murray-Wallace, C.V., Belperio, A.P., Cann, J.H., 1998. Quaternary neotectonism and intra-plate volcanism: the Coorong to Mount Gambier Coastal Plain, Southeastern Australia: a review. In: Vita Finzi, C., Stewart, C.Ż. (Eds.), Coastal Tectonics. Geological Society, London, pp. 255–267.
Murray-Wallace, C.V., Brooke, B.P., Cann, J.H., Belperio, A.P., Bourman, R.P., 2001. Whole rock aminostratigraphy of the Coorong Coastal Plain, South Australia: towards a 1 million year record of sea-level highstands. J. Geol. Soc. Lond. 158, 111–124.
Mylroie, J.E., 2008. Late Quaternary Sea-level position: evidence from Bahamian carbonate deposition and dissolution cycles. Quat. Int. 183, 61–75.
Nathan, R.P., Mauz, B., 2008. On the dose-rate estimate of carbonate-rich sediments for trapped charge dating. Radiat. Meas. 43, 14–25.
Olley, J.M., Murray, A.S., Robert, R.G., 1996. The effects of disequilibria in the uranium and thorium decay chain on burial dose rates in fluvial sediments. Quat. Sci. Rev. 15, 751–760.
Olson, S.L., Hearty, P.L., 2009. A sustained +21 m sea-level highstand during MIS 11 (400 ka): Direct fossil and sedimentary evidence from Bermuda. Quat. Sci. Rev. 28 (3–4), 271–285.
Oppo, D.W., Fairbanks, R.G., Gordon, A.L., 1990. Late Pleistocene Southern Ocean N13C variability. Paleoceanography. 5, 43–54.
Pappu, S., Gunnell, Y., Akhilesh, K., Baucher, R., Taieb, M., Demory, F., Thouveny, N., 2011. Early Pleistocene presence of Acheulian Hominins in South India. Science. 331 (6024), 1596–1599.
Pillans, B., 2003. Subdividing the Pleistocene using the Matuyama-Brunhes boundary (MBB): an Australian perspective. Quat. Sci. Rev. 22, 1569–1577.
Polymeris, G.S., Erginal, A.E., Kiyak, N.G., 2012. A comparative morphological, compositional and TL study of Tenedos (Bozcaada) and Şile aeolianites, Turkey. Mediter. Archaeol. Archaeom. 12 (2), 117–131.
Porat, N., Botha, G., 2008. The luminescence chronology of dune development on the Maputaland coastal plain, Southeast Africa. Quat. Sci. Rev. 27, 1024–1046.
Porat, N., Wintle, A.G., 1995. IRSL dating of aeolianites from the Late Pleistocene coastal kurkar ridge, Israel. Alfred Wegner Stiftung, Berlin.
Prescott, J.R., Hutton, J.T., 1988. Cosmic ray and gamma ray dosimetry for TL and ESR. Nucl. Tracks Rad. Meas. 14, 223–227.
Prescott, J.R., Hutton, J.T., 1994. Cosmic ray contribution to dose rates for luminescence and ESR dating: large depths and long-term time variations. Radiat. Meas. 23, 497–500.
Price, D.M., Brooke, B.P., Woodroffe, C.D., 2001. Thermoluminescence dating of aeolianites from Lord Howe Island and south-west Western Australia. Quat. Sci. Rev. 20, 841–846.
Roberts, D.L., Bateman, M.D., Murray-Wallace, C.V., Carr, A.S., Holmes, P.J., 2008. Last interglacial fossil elephant trackways dated by OSL/AAR in coastal aeolianites, still Bay, South Africa. Palaeogeogr. Palaeoclimatol. Palaeoecol. 257, 261–279.
Rodríguez-López, J.P., Clemmensen, L.B., Lancaster, N., Mountney, N.P., Veiga, G.D., 2014. Archean to recent aeolian sand systems and their sedimentary record: current understanding and future prospects. Sedimentology 61 (6), 1487–1534.
Rohling, E.J., Braun, K., Grant, K., Kucera, M., Roberts, A.P., Siddall, M., Trommer, G., 2010. Comparison between Holocene and Marine Isotope Stage-11 sea level histories. Earth Planet Sci. Lett. 291 (1–4), 97–105.
Rousseau, D.D., Puissegur, J.J., Le Colle, F., 1992. West-European terrestrial molluscs assemblages of isotopic stage 11 (Middle Pleistocene): climate implications. Palaeogeogr. Palaeocl. 92, 15–29.
Rowe, M.P., Bristow, C.S., 2015. Landward-advancing Quaternary eolianites of Bermuda. Aeolian Res. 19 (B), 235–249.
Sayles, R.W., 1931. Bermuda during the ice age. Proc. Am. Acad. Arts Sci. 66, 381–467.
Shackleton, N., 1987. Oxygen isotopes, ice volume and sea level. Quat. Sci. Rev. 6 (3–4), 183–190.
Shackleton, N.J., Berger, A., Peltier, W.R., 1990. An alternative astronomical calibration of the lower Pleistocene timescale based on ODP Site 677. Earth Environ. Sci. Trans. R Soc. 81 (4), 251–261.
Siddall, M., Chappell, J., Potter, E.K., 2006. Eustatic sea level during past interglacials. In: Sirocko, F., Clausses, M., Sanchez Goni, M.F., Litt, T. (Eds.), The Climate of Past Interglacials. Elsevier, Amsterdam.
Sivan, D., Porat, N., 2004. Evidence from luminescence for late Pleistocene formation of calcareous aeolianite (kurkar) and paleosol (hamra) in the Carmel Coast, Israel. Palaeogeogr. Palaeocl. 211 (1–2), 95–106.

Sivan, D., Gvirtzman, G., Sass, E., 1999. Quaternary stratigraphy and paleogeography of the Galilee coastal plain, Israel. Quat. Res. 51 (3), 280–294.
Stirling, C.H., Esat, T.M., Lambeck, K., McCulloch, M.T., Blake, S.G., Lee, D.C., Halliday, A.N., 2001. Orbital forcing of the marine isotope stage 9 interglacial. Science. 291 (5502), 290–293.
Sun, Y., Clemens, S.C., An, Z., Yu, Z., 2006. Astronomical timescale and palaeoclimatic implication of stacked 3.6-Myr monsoon records from the Chinese Loess Plateau. Quat. Sci. Rev. 25 (1–2), 33–48.
Svitoch, A.A., Selivanov, A.O., Yanina, T.A., 2000. Paleohydrology of the Black Sea Pleistocene basins. Water Res. 27 (6), 594–603.
Tsatskin, A., Ronen, A., 1999. Micromorphology of a Mousterian paleosol in aeolianites at the site Habonim, Israel. Catena. 34 (3–4), 365–384.
Tsatskin, A., Sandler, A., Avnaim-Katav, S., 2015. Quaternary subsurface paleosols in Haifa Bay, Israel: a new perspective on stratigraphic correlations in coastal settings. Palaeogeogr. Palaeocl. 426, 285–296.
Vandenberghe, J., 2000. A global perspective of the European chronostratigraphy for the past 650 ka. Quat. Sci. Rev. 19 (17–18), 1701–1707.
Vezina, J., Jones, B., Ford, D., 1999. Sea level highstands over the last 500 000 years: evidence from the Ironshare Formation on Grand Cayman, British West Indies. J. Sediment. Res. 69 (2), 317–327.
Wegwerth, A., Dellwig, O., Kaiser, J., Ménot, G., Bard, E., Shumilovskikh, L., Schnetger, B., Kleinhanns, I.C., Wille, M., Arz, H.W., 2014. Meltwater events and the Mediterranean reconnection at the Saalian-Eemian transition in the Black Sea. Earth Planet Sci. Lett. 404, 124–135.
Xu, H., Liu, B., Wu, F., 2010. Spatial and temporal variations of Rb/Sr ratios of the bulk surface sediments in Lake Qinghai. Geochem. Trans. 11 (3), 1–8.
Yanko-Homback, V., Schnyukov, E., Pasynkov, A., Sorokin, V., Kuprin, P., Maslakov, N., Montnenko, I., Smyntyna, O., 2017. In: Flemming, N.C., Harff, J., Moura, D., Burgess, A., Bailey, G.N. (Eds.), Geological and Geomorphological Factors and Marine Conditions of the Azov-Black Sea Basin and Coastal Characteristics as they Determine Prospecting for Seabed Prehistoric Sites on the Continental Shelf, Submerged Landscapes of the European Continental Shelf: Quaternary Paleoenvironments, First edition. Wiley Blackwell, Oxford, pp. 431–478.
Yildirim, C., Melnick, D., Ballato, P., Schildgen, T.F., Echtler, H., Erginal, A.E., Kıyak, N. G., Strecker, M.R., 2013. Differential uplift along the northern margin of the Central Anatolian Plateau: Inferences from marine terraces. Quat. Sci. Rev. 81, 12–28.
Yu, P.S., Chen, M.T., 2011. A prolonged warm and humid interval during marine isotope stage 13–15 as revealed by hydrographic reconstructions from the South China Sea (IMAGES MD972142). J. Asian Earth Sci. 40, 1230–1237.
Zaineldeen, U.F., 2010. Palaeowind estimation of cross-bedding within the aeolian Kurkar layers of the Gaza Formation, Gaza Strip, Palestine. Geol. Croat. 63 (1), 55–65.
Zhao, Q., Wu, S., Xu, H., Sun, Q., Wang, B., Sun, Y., Cao, F., He, X., 2011. Sedimentary facies and evolution of aeolianites on Shidao Island, Xisha Islands. Chin. J. Oceanol. Limnol. 29 (2), 398–413.
Zimmerman, D.W., 1971. Thermoluminescence dating using fine grains from pottery. Archaeometry 13, 29–52.
Vandenberghe, J., An, Z.S., Nugteren, G., Lu, H., Van Huisste- den, J., 1997. New absolute time scale for the Quaternary climate in the Chinese loess region by grain-size analysis. Ž Geol. 25 (1), 35–38.